Influence of the modelling properties on the seismic response of free-standing spent fuel racks

Alberto González Merino[a,b], Luis Costas[a], Arturo González[b]

[a]*Equipos Nucleares, S.A., Avda. Juan Carlos I / 8, Maliaño 39600, Spain*
[b]*University College Dublin, School of Civil Engineering, Dublin 4, Ireland*

* Corresponding author. Tel.: +34-942-200-101; fax: +34-942-200-148
E-mail address: gonzalez.alberto@ensa.es

Abstract

Free-standing racks are metallic structures designed to store fuel assemblies in the spent fuel pool. Their seismic analysis deals with complex physical phenomena such as transient motion, inertial effects, dynamic contacts, fluid-structure interaction, water coupling, etc. The associated computational effort leads to cost-effective finite element models made up of simple elements: beams, masses and contacts. The modelling properties that describe the physical behaviour of such conceptual elements are uncertain and difficult to estimate. However, they have a certain impact on the computation of the rack response. This paper investigates the weight of the main modelling properties on computed outcomes focusing on sliding displacements and reactions on supports. The conceptual approach is supported with a statistical analysis of 100 simulations conducted in ANSYS Mechanical 14.0. A multivariate sensitivity analysis with scatter plots and variance-based methods is conducted over modelling variables including friction coefficients, contact stiffnesses, assumed fuel gaps, inertias, etc. Furthermore, some advises and rule of thumbs are provided for future designs.

Keywords: free-standing racks, seismic analysis, modelling, sensitivity, Sobol.

1 Introduction to the rack seismic problem

Spent fuel racks store irradiated fuel elements during the first step of the nuclear waste management process. Rack units consist of an array of parallelepiped storage cells that are vertically filled with fuel assemblies. Rack units rest free-standing on the depths of the spent fuel pool submerged in water and spaced by a few centimeters. During an earthquake, pool accelerations are transmitted to the rack units through frictional forces on supports and compression of the water volume. The whole rack system is then subjected to inertial and viscous forces as well as a fluid-structure interaction.

Hence, rack units undergo large 3D displacements (e.g. sliding, rocking, twisting and turning) delimited by the pool boundaries. The rack response combines therefore three main modes of motion: (a) movement stuck to the pool floor, (b) sliding displacement over the pool liner and (c) rocking oscillation around their vertical position. Such a combination is in continuous change (Queval et al. 1999). Sliding and rocking motions alternate or take simultaneously place when friction forces reach saturation and the balance of moments gets destabilized by eccentric forces. The general equation of motion (Eq. 1) describes the overall response, but it is implicitly affected by many modelling variables as the contact features or the fuel assumptions.

$$[M]\{\ddot{u}(t)\} + [C]\{\dot{u}(t)\} + [K]\{u(t)\} = \{F_{seism}(t)\} + \{F_{fluid}(t)\} + \{F_{weight}\} \quad (1)$$

where [*M*], [*C*] and [*K*] are the mass, damping and stiffness matrices of the structural system respectively while {u(t)}, {u̇(t)} and {ü(t)} are vectors containing the translational and rotational degrees of freedom of the structure and their respective velocities and accelerations. The right side of the equation refers to the external forces applied at each nodal degree of freedom. $\{F_{seism}(t)\}$ and $\{F_{fluid}(t)\}$ are the time-dependent vectors relative to the seismic excitation and the Fluid-Structure Interaction forces. Finally, $\{F_{weight}\}$ represents the underwater self-weight of the rack structure and the fuel loading.

2 Ad-hoc modelling of the rack system

2.1 Typical 2-rack seismic model

Cost-effective finite element (FE) models are required to deal with the computational cost of the rack seismic analysis. Since the last is directly proportional to the number of nodes involved in the matrices of Equation 1, simplifications are needed to keep the number of nodes as low as possible. However, the rack seismic model must be able to accurately simulate the main 3D motions of the system, including the rack slidings displacements, the rack rocking oscillations with support uplifts and the fuel rattling among others. Several modelling approaches have been developed in different softwares during the last decades (Champomier et al., 1989, 2001; Ashar and Degrassi, 1989; Degrassi, 1992; Zhao et al., 1996; Zhao 1997; Hinderks et al., 2000). Figure 1 represents the typical 2-rack seismic model used in the present investigation. Such a conceptual model is built in ANSYS Mechanical 14.0 (ANSYS, 2013) and combines mass and beam elements with dynamic contacts and hydrodynamic couplings.

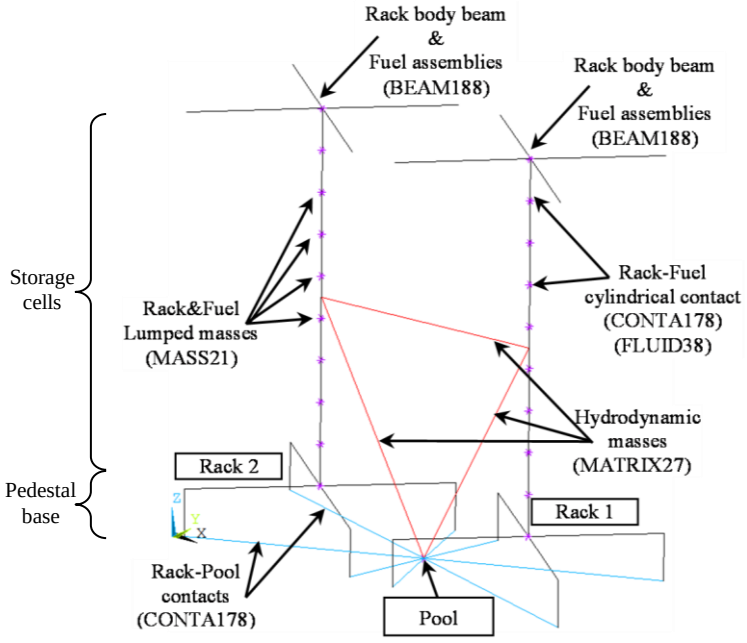

Figure 1 Finite Element model used in the transient seismic analysis

The seismic loading is directly input as an acceleration-time history at the pool node. It follows the latest recommendations (ANSYS, 2012) in order to facilitate the integration, prevent errors in the computation of nodal accelerations (Gonzalez et al., 2017) and avoid the discontinuities raised by the traditional displacement-time stories method (Lee et al., 1998). In addition, the external forces of the Fluid-Structure Interaction are replaced by added masses (Fritz, 1972; Chung and Chen, 1976). The application of the hydrodynamic mass concept is considered cost-effective (Soler and Singh, 1982). Hence, Equation 1 becomes Equation 2:

$$\left[M + m_{hydro}\right]\{\ddot{u}(t)\} + [\alpha M + \beta K]\{\dot{u}(t)\} + [K]\{u(t)\} = \{F_{weight}\} \qquad (2)$$

Where the seismic forces are included as pool acceleration-time history in the {ü(t)} vector and the fluid forces are replaced by added masses [m_{hydro}]. The viscous damping matrix is approached by a linear combination of mass and stiffness matrices according to the where α and β are the respective Rayleigh constants of proportionality. The external forces of the right side of the equation are then reduced to the underwater self-weight of the rack and fuel.

2.2 Rack units

Rack units are shaped by a pedestal base and a vertical cantilever beam. The pedestal is made up of four support feet connected to a rigid frame. The cantilever body beam represents the ensemble of storage cells of the rack unit. All structural elements are one-dimensional (ANSYS BEAM188) and massless. The total rack mass is lumped into mass elements (ANSYS MASS21) at 10 different levels according to a parametric analysis of the Finite Element

nodalization (Gonzalez et al.; 2017). The cross sectional areas of the beam elements are specified to replicate the vertical and horizontal natural frequencies of the real rack units.

2.3 Fuel assemblies

Since the different fuel assemblies are assumed to rattle in phase inside their respective storage cells, they are modelled grouped as a single vertical beam (ANSYS BEAM188) collinear with the rack body beam. Both beams are modelled separated by a constant gap along the rack height and connected at multiple levels through cylindrical contacts (ANSYS CONTA178) and dynamic fluid coupling elements (ANSYS FLUID38). The total fuel mass is lumped into mass elements (ANSYS MASS21) at those levels and the cross sectional area of the equivalent fuel beam is specified to replicate the dynamic properties of the bunch of assemblies.

2.4 Dynamic contact elements

Multiple contact events appear and disappear throughout the rack seismic analysis. The alternating liftings of the rack supports from the pool floor caused by the rack rocking and the rattling motion of the fuel assemblies within the storage cell represent the main source of nonlinearities. They cause abrupt changes in the stiffness matrix [K] at the beginning and end of the impact events. In addition to the convergence difficulties associated to these chattering discontinuities, spurious high frequency oscillations may be trigger while the stiff contact is active.

In order to mitigate the difficulties of the analysis, dynamic contacts are usually softened according to the penalty-based method. Contact elements are then modelled as compression-only spring elements allowing a slight penetration along interfaces. Impacts become then elastic so the reaction force is linearized from zero just before the impact to its peak at the maximal penetration. Moreover, velocity is progressively adapted reducing the Gibbs ripple and enforcing energy conservation. Transmission of tensile forces is disabled since the contact gap capability provides for opening and closing interfaces. However, contact penetration artificially softens the contact surface which reduces the impact force and increases the impact duration. Hence, penetration effects must be studied carefully to ensure that accuracy is not sacrificed in favour of easier convergence. It is recommended to use the smallest penetration that removes the spurious high frequency oscillations and converges to an accurate result.

Similarly, frictional forces opposing the relative motion along the interface also appear and disappear when the contact is closed or open respectively. They give rise to hysteretic energy losses emphasizing the nonlinear response. Contact elements approach these frictional effects through a simple Coulombian model where friction forces are calculated as the product of the friction coefficient by the normal contact reaction. They peak then at the maximal penetration where the contact force reaches its maximum. Experimental tests for stainless steel contacts in underwater conditions pointed out a wide dispersion in the friction coefficients, going from 0.2 to 0.8 (Rabinowicz, 1976). Hence, it is current practise to ignore the slight difference between static and dynamic friction and to assume the same coefficient for both frictions.

2.5 Hydrodynamic coupling elements

Besides the buoyancy vertical force, the water volume affects the dynamic response of every submerged solid and alters their individual natural frequencies. Actually, the fluid-structure interaction induces a significant action over all the in-motion structures including the fuel assemblies stored inside the cells and the racks themselves inside the pool. It opposes the relative motion between wet boundaries creating coupling forces that push for an in-phase motion (Soler and Singh, 1984). The magnitude of this 'water coupling effect' depends on the geometrical shape of the racks and the size of the clearance space between units. Actually, it increases exponentially when the units get closer. This effect is approached through the aforementioned hydrodynamic mass concept which replaces the water action by an equivalent modification of the element mass matrix [M]. It must be noted that the hydrodynamic mass matrix [m_{hydro}] is calculated only once for the initial layout of the pool as opposed to a continuous updating throughout the time history according to transient displacement of racks. It assumes a nearly in-phase motion of the rack units with small relative displacements. It is considered a safe assumption since any large relative displacement between rack units will reduce the thickness of the water gaps in-between boosting the water coupling effect.

This model implements ANSYS MATRIX27 elements connecting racks and pool in order to specify the previously-computed added masses. Similarly, ANSYS FLUID38 elements connect the fuel assemblies and the rack body beam to specify the hydrodynamic coupling brought by the water volume trapped in the annular gap of the storage cell.

3 Sensitivity analysis of the main modelling properties

3.1 Design of experiments and input sampling

The Design of Experiments (DoE) includes one hundred numerical simulations conducted on the 2-rack model shown in Figure 1 for a scale 1/3 mock-up used for experimental testing. It follows the Latin Hypercube Sampling (LHS) to effectively explore the multidimensional input space. Wide uniform distributions are preliminary assumed in order to take into account random uncertainties. The variables with potential influence on the computed results are listed together with their range of variation in Table 1 for ease of reference.

Table 1: Set of variables of the input space

	Variables	*Units*	*Min*	*Max*
Input data	Earthquake accelerogram	m^2/s	*See Figure 2	
	Rack mass	kg	630	
	Fuel mass	kg	2500	
	Eigen-frequency in X	Hz	10	
	Eigen-frequency in Z	Hz	90	
	Hydrodynamic masses factor	%	100	
Modeling properties	Rack-Pool friction coefficient	-	0.2	0.8
	Rack-Pool contact stiffness	N/m	1E+05	1E+10
	Fuel-Cell contact stiffness	N/m	1E+04	1E+09
	Fuel-Cell gap	mm	1	10
	Fuel beam inertia	m^4	8.3E-10	8.3E-06
Solution controls	Maximum allowed step size ('DELTIM')	s	6E-04	
	Number of equilibrium iterations ('NEQIT')	#	5	
	Convergence parameter ('CNVTOL')	m	5E-06	
	Amplitude decay factor ('TINTP')	-	0,05	
	Rayleigh mass proportional damping ('ALPHAD')	%	0	
	Rayleigh stiffness proportional damping ('BETAD')	%	5	

Since this paper focus on the influence of the modelling properties, only the uncertain variables related to friction coefficient, contact stiffnesses, fuel-cell gaps and fuel rigidity are varied. Input data and solution controls are set at their nominal values. The acceleration time-history of reference is provided in Figure 2. It lasts around 12 seconds with peaks up to ±8 m/s^2 reaching velocities up to 0.7 m/s. A low excitation starting interval (0-2 seconds) is followed by high excitation shakings (2-8 seconds) which progressively blow out during the last 2 seconds.

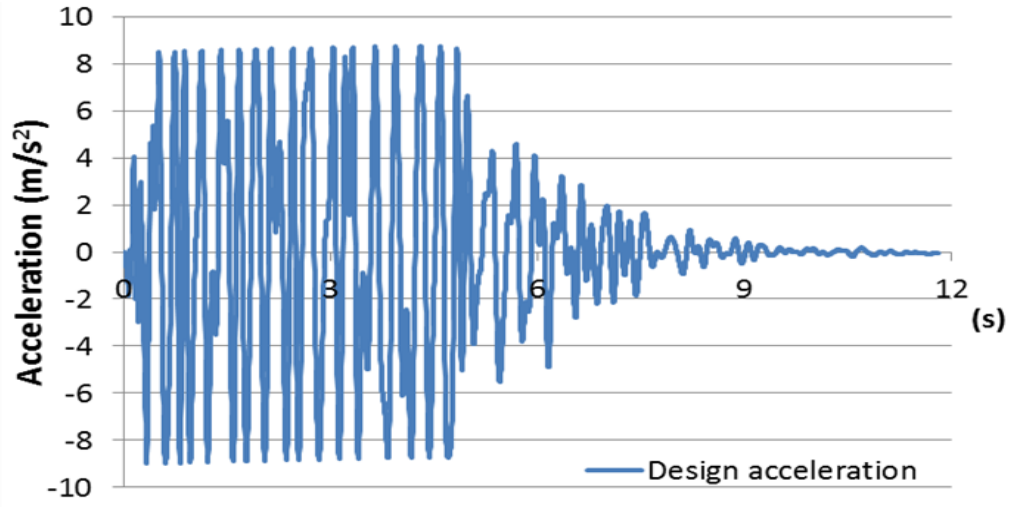

Figure 2 Design acceleration-time history

The transient analysis carries out a full 3D implicit time integration of the differential equation of motion (Eq. 2) at multiple time steps. In other words, the analysis is discretised into short time steps where the system equilibrium is enforced. The HHT algorithm (Hilbert, Hubert and Taylor, 1977) with a high amplitude decay factor is chosen for the numerical integration. An adaptive time stepping scheme automatically changes the step size as the calculation proceeds in order to achieve convergence. Iterative series of Newton-Raphson linear approximations gradually approach nonlinearities by updating the tangent stiffness matrix at each equilibrium iteration. Rayeigh viscous damping is assumed with a 5% structural damping flat fee consistent with the regulatory authorities (USNRC, 1981).

3.1.1 Rack-Pool friction coefficient

The friction coefficient has a strong influence in the relative motion of the rack units over the pool liner. Moreover, it plays a decisive role in the rack rocking motion since the torque of its eccentric leverage affects the momentum balance. Hence, while low friction levels allow for large sliding displacements, high frictions lead to a coupled response. In the latter, rack supports follow the pool horizontal motion but the rack body tends to tilt at each sharp change in the acceleration. This is evidenced in Figure 3, where the relationship between friction coefficient and maximum supports uplift is plotted for the 100 simulations. Then, a conservative friction value cannot be therefore prescribed a priori and separate analyses are currently required to consider a maximum sliding case and a maximum rocking case respectively. Regarding the computational cost, Figure 4 shows that rocking is cheaper to analyse than sliding as contact elements are less time active. Indeed, Figure 5 points out that a high friction coefficient increases the mean step size and reduces the number of required equilibrium iterations.

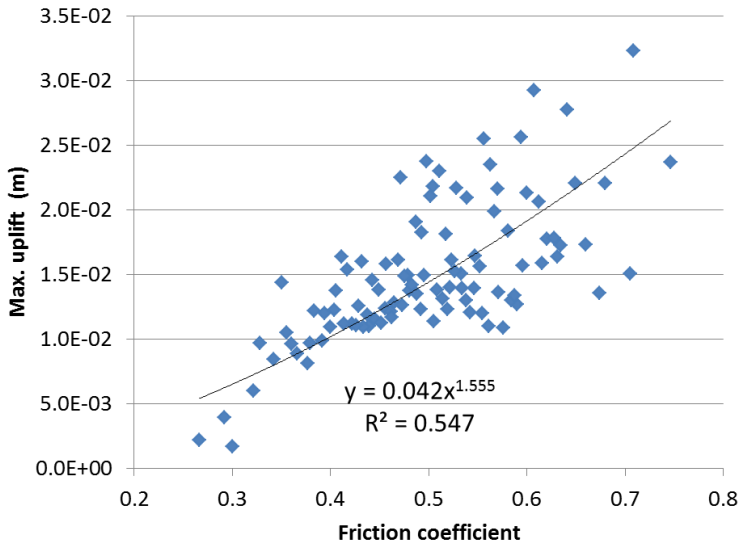

Figure 3 Relationship between friction coefficient and maximum uplift of the rack support

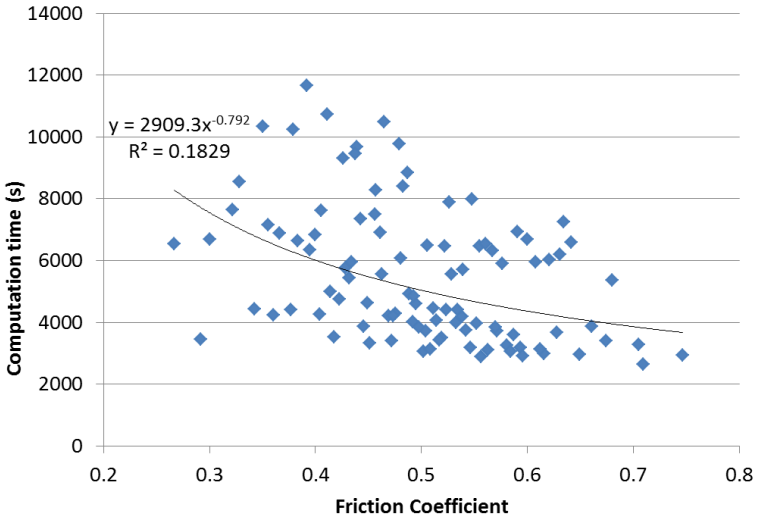

Figure 4 Relationship between friction coefficient and computation time

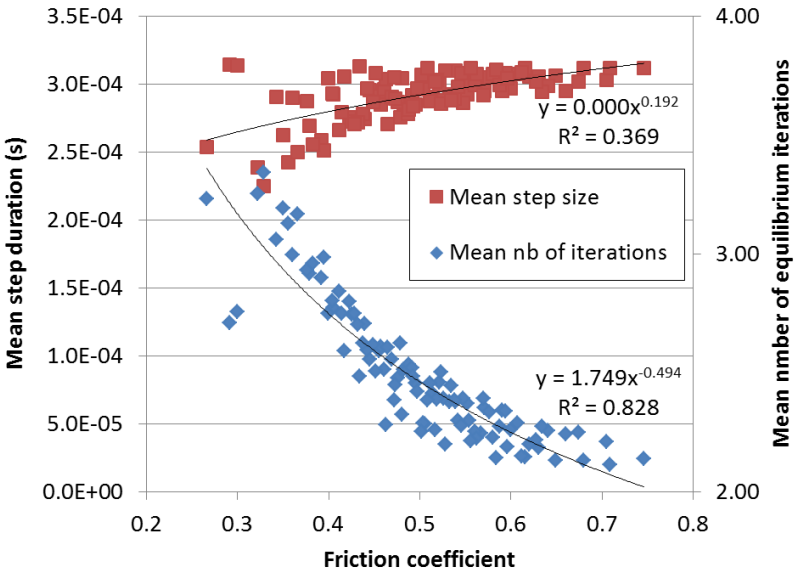

Figure 5 Relationship between friction coefficient and mean step size

3.1.2 Rack-Pool contact stiffness

The rack-pool contact stiffness determines the roughness of the vertical impacts generated when the rack supports lift up and sink into the pool floor during rocking oscillations. Contact stiffness determines the penetration and therefore duration of the impulse and the energy exchange associated to the impact. Stiff contacts lead to high peak impact forces over a short period of time whereas soft contacts go on for longer durations with smaller peaks. The former minimizes interpenetration of surfaces, whereas the latter mitigates discontinuity and facilitates analysis convergence. Figure 6 shows the influence of the rack-pool contact stiffness on the mean step duration.

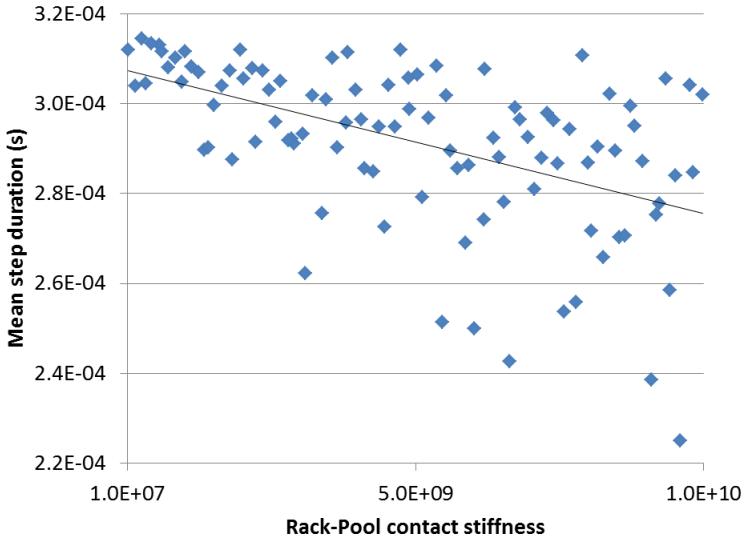

Figure 6 Relationship between Rack-Pool contact stiffness and the mean step size

3.1.3 Fuel-Cell contact stiffness

The fuel-cell contact stiffness determines the roughness of the horizontal impacts between fuel assemblies and their storage cells. Fuel assemblies rattle inside the storage cell alternatively hitting the walls in their swinging motion. Since the fuel firstly impacts on the top of the rack body beam, their momentum leverage strongly contributes to the rocking behaviour of the rack unit. Stiff contacts contribute to 'knocking' events (i.e. discrete impulses) whereas soft contacts lead to an extended 'pushing' action where fuel inertial effects join the rack mass all over the rack height. Figure 7 shows the increase in the maximal impact force associated to the stiffness of the fuel-cell contact.

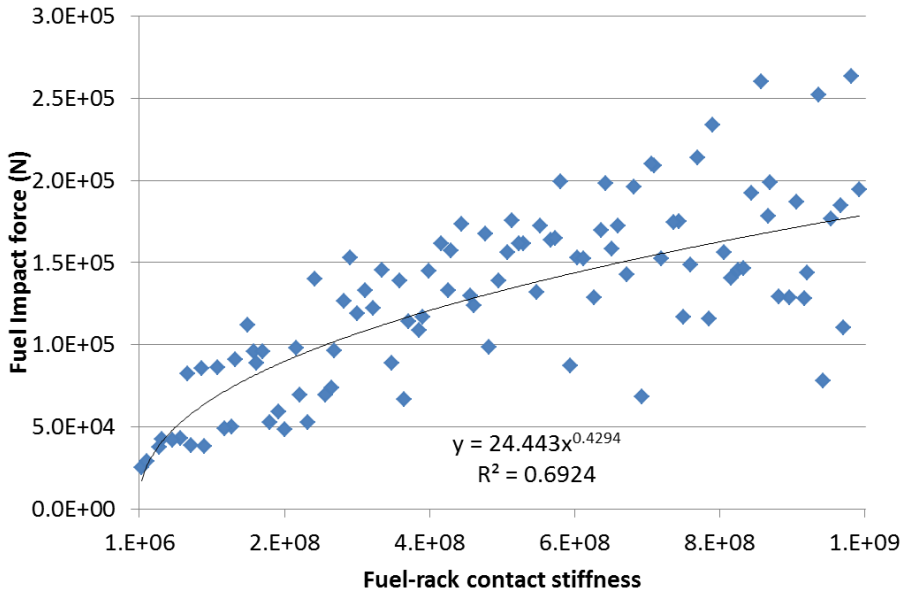

Figure 7 Relationship between Fuel-Cell contact stiffness and their associated maximal horizontal force

3.1.4 Fuel-Cell gap

The annular gap between the fuel assembly and the storage cell influences the magnitude and recurrence of the impact events. It limits the amplitude of the fuel oscillations and therefore the maximal relative velocity reachable before impact. Figure 8 shows that small gaps lead to frequent minor impacts, whereas large gaps lead to rare but strong impact forces due to bigger inertial effects of the fuel mass.

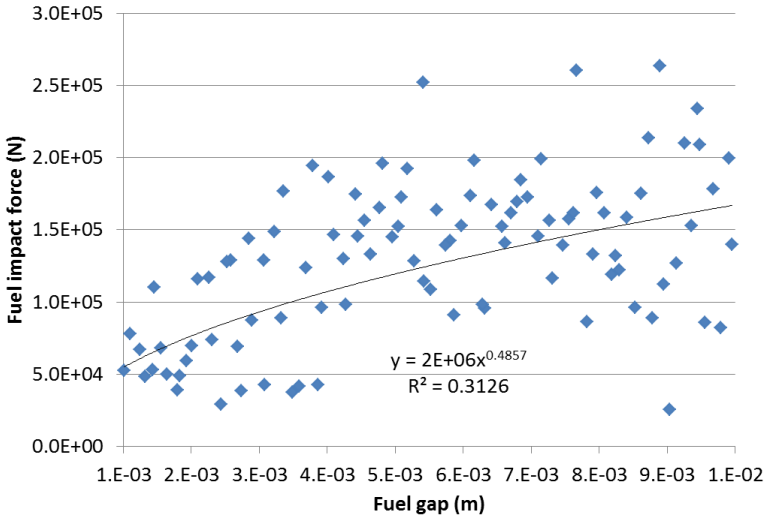

Figure 8 Relationship between Fuel-Cell contact stiffness and their associated maximal horizontal force

3.1.5 Fuel beam rigidity

The flexural rigidity of the fuel element represents its ability to deform after hitting the cell wall. It affects not only the roughness of the impacts but also the number of contacts activated along the rack body beam. Rigid assemblies cause well-defined impacts at the top of the rack body, whereas flexible assemblies deform up to stick to the cell wall creating a contact area pressure. Hence, resonances between fuel and rack oscillations can temporary occur for some excitation frequencies (Oh and Ryu, 2013).

3.2 Transient results and envelop curves

The response of the rack system is affected by the aforementioned modelling properties. The range of variation throughout the seismic event provides a straightforward insight into the robustness of the seismic analysis across time. Upper and lower envelope curves of the 100-simulation sample are provided in Figures 9 and 10 for the sliding displacements and the vertical forces on support respectively. These graphs also plot the evolution along time of the mean and the standard deviation of the experiments as a measure of dispersion. The envelopes represent deviations from the mean of up to 10 times the standard deviation for the sliding displacements and between -6.6 and 9.4 for the reaction forces.

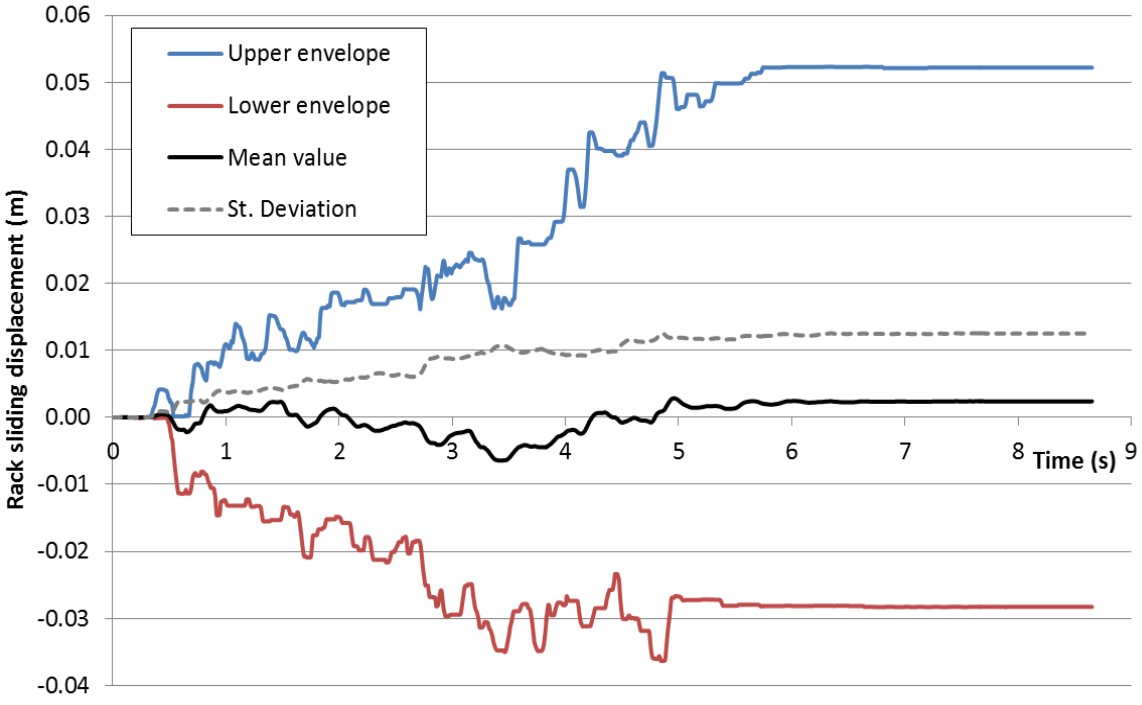

Figure 9. Envelopes of the rack sliding displacements associated with uncertain modelling properties

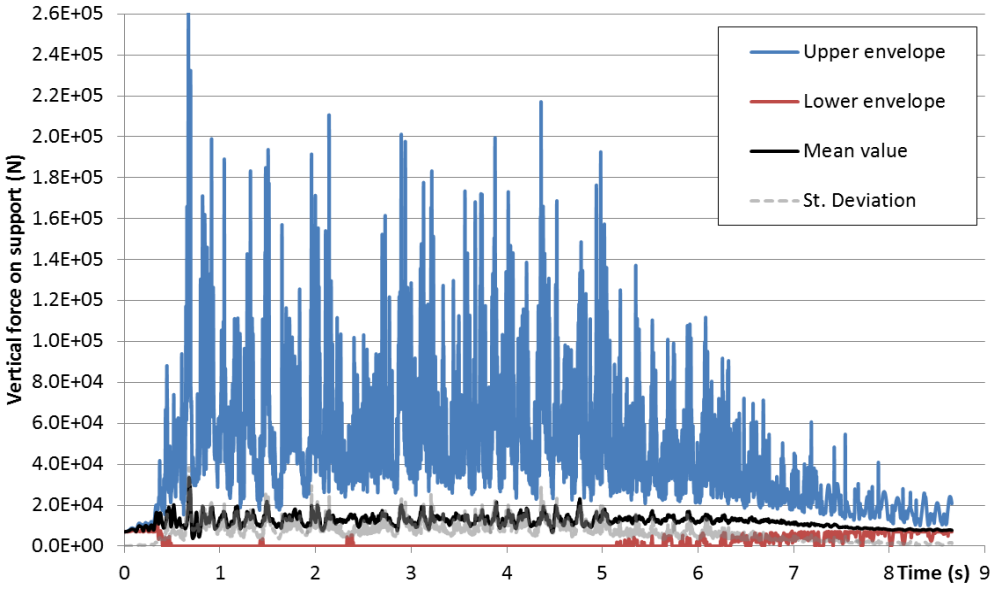

Figure 10. Envelopes of the vertical forces on supports associated with uncertain modelling properties

3.3 Statistical distribution of the key outputs

Transient responses can be filtered to obtain quantitative output data. The maximum sliding displacements and maximum reactions on support are compiled for the 100-simulation sample. Their respective Probability Density Function (PDF), Cumulative Distribution Function (CDF) and relevant descriptive statistics are shown in Figure 11 and Figure 12. The Coefficient of Variation (CV), defined as the ratio of the standard deviation to the mean, is a standardized measure of dispersion that provides insight about the uncertainty of the outputs. It is noted that it is much higher for the sliding displacements (CV= 1.270) than for the vertical reaction on support (CV=0.297).

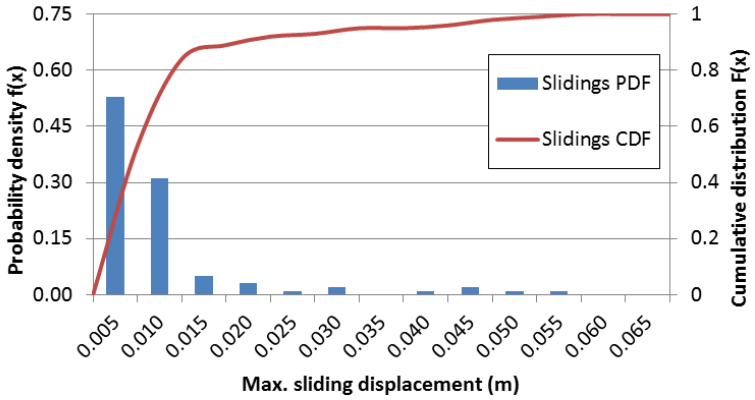

Number of simulations	100
Mean (m)	7.714E-03
Standard Deviation	9.800E-03
Min. Value (m)	7.974E-06
Max. Value (m)	5.231E-02
90th Percentile (m)	1.660E-02
95th Percentile (m)	2.591E-02
99th Percentile (m)	4.843E-02

Figure 11 Maximum sliding displacement

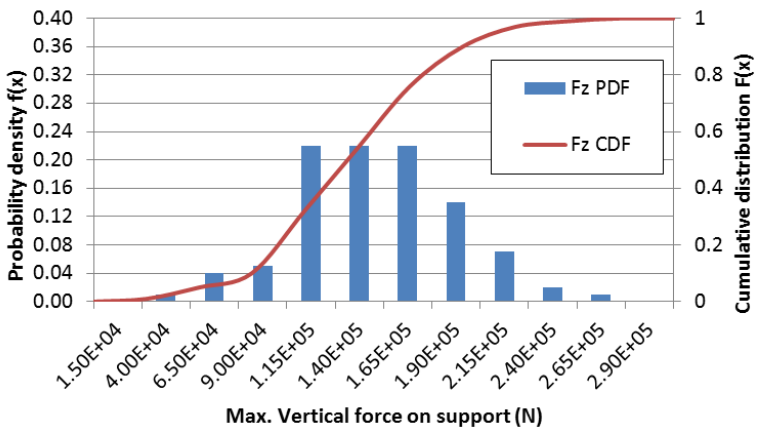

Number of simulations	100
Mean (N)	1.357E+05
Standard Deviation	4.031E+04
Min. Value (N)	3.711E+04
Max. Value (N)	2.632E+05
90th Percentile (N)	1.894E+05
95th Percentile (N)	1.985E+05
99th Percentile (N)	2.329E+05

Figure 12 Maximum vertical force on support displacement

3.4 Scatter plots

The scatter plots of Figure 13 display output data as a collection of points in order to identify the influence of the aforementioned modelling properties on the maximum sliding displacement of racks and on the maximum vertical

force on supports. The screening of these dot distributions covers the whole input space described in Table 1 highlighting the positive, negative or null correlation between inputs and outputs across the input space.

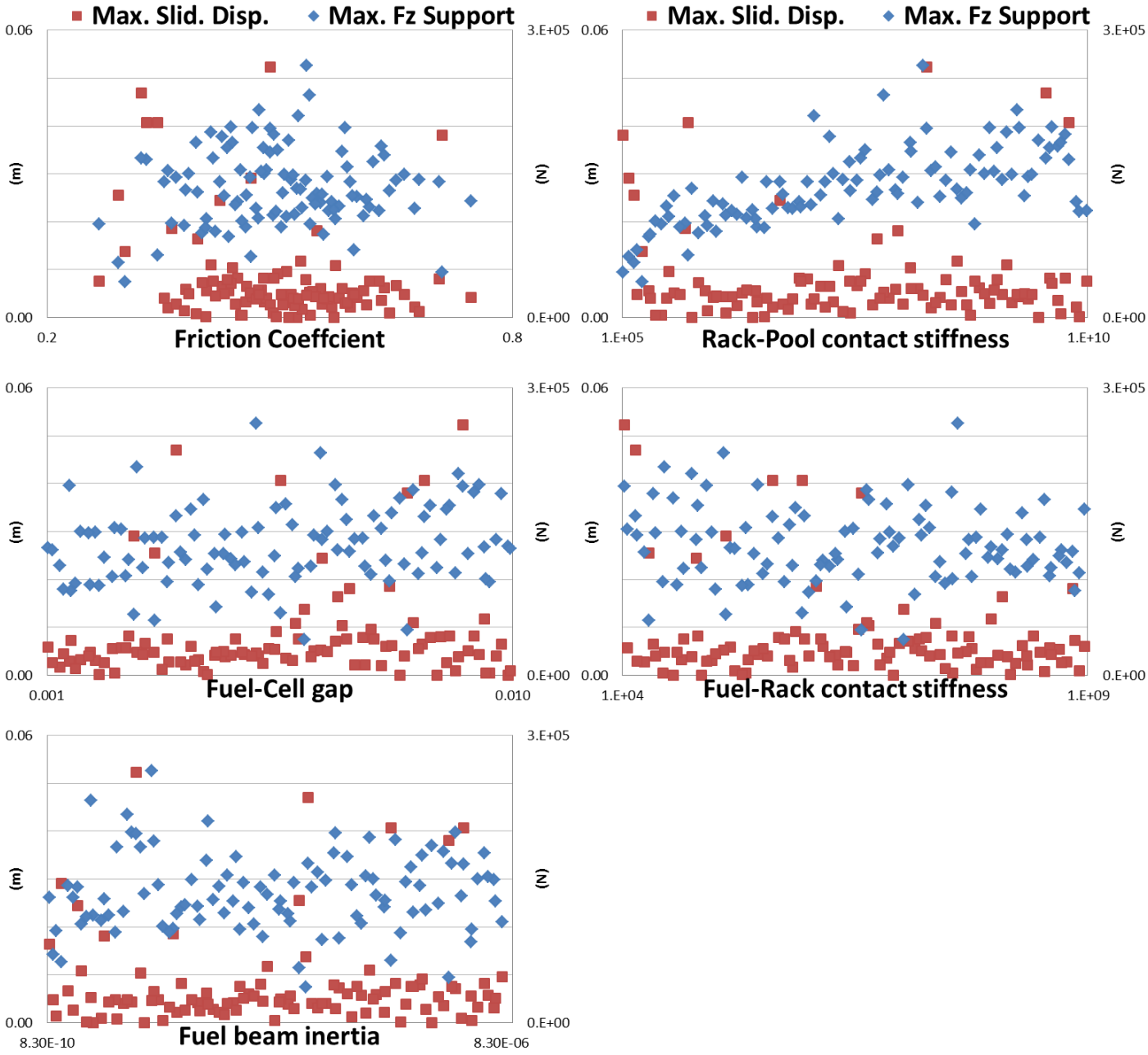

Figure 13 Scatter plots: Modelling properties vs. maximum sliding displacements and vertical force on supports

The maximal sliding displacement generally remains under 1cm, but for some cases it may exceed 5cm. Such a dispersion decreases for high values of fuel-cell contact stiffness as noted by the triangular shape of the red dots distribution.

The impact forces on support range between 37 and 263kN instead. The uniform spread distributions of the blue dots indicate their low sensitivity to the fuel-cell gap and fuel beam inertia. However, stronger dependences to the contact stiffness are noticed. Forces on support linearly increase with the stiffness allocated to the rack-pool contact whereas they slightly decrease with the fuel-cell contact stiffness.

4 Surrogate modelling for multivariate sensitivity analysis

Synthetic mathematical relationships between input and output sets of data can be inferred though Polynomial Chaos Expansions (PCE). The resulting surrogate models are cost-effective in the prediction of outputs with certain

accuracy. In this way, three independent surrogate models are built to approach each of the three outputs of interest. Their respective regression coefficients are provided on Table 2.

Table 2 Validation metrics of the surrogate models for uncertain modelling properties

		Max. Slid. Displ.	**Max. Fz on support**	**CPU Time**
S	Number of simulations	100	100	100
Res	Residual	0.0005	1966	124.9
R2	Coefficient of determination	0.7363	0.7597	0.6680

The residual value represents a measure of the mean error in the fitting of the surrogate model. Since R2 circle the standard threshold of 0.7 the three surrogate models can be accepted. However, although the prediction accuracy might be further discussed, the general patterns and trends of their outcomes are considered reliable enough. Hence, these surrogate models are useful to conduct a multivariate sensitivity analysis where all the analysis properties vary at the same time. Table 3 summarizes the influence of each analysis parameter on the three outputs of major interest. The general impact is described on the second column by upward or downward arrows whereas the coupled effect whether two variables are combined is provided on the right hand columns: reinforced (+), similar (=), or blurred (-). A double notation sign is allocated to critical combinations where the primary effect can be overturned.

Table 3: Influence of the main modelling properties on the key final outputs

Modelling properties		Primary effect		Coupled effect				
				FC↑	R-C contact stiffness↑	F-R contact stiffness↑	Fuel gap↑	Fuel beam rigidity↑
Friction Coefficient	↑	Max. Slid. Disp.	↓		-	=	-	=
		Max. Fz Support	↑		+	=	+	=
		CPU Time	↓		+	+	=	++
Rack-Pool Contact Stiffness	↑	Max. Slid. Disp.	↓	-		++	=	++
		Max. Fz Support	↑	+		=	=	=
		CPU Time	↑	+		++	=	=
Fuel-Cell Contact Stiffness	↑	Max. Slid. Disp.	↓	=	++		++	+
		Max. Fz Support	↓	+	+		+	=
		CPU Time	↓	+	--		++	+
Fuel-Cell gap	↑	Max. Slid. Disp.	↑	+	+	--		++
		Max. Fz Support	↓	-	+	=		=
		CPU Time	↓	=	=	++		=
Fuel beam rigidity	↑	Max. Slid. Disp.	↓	=	+	+	--	
		Max. Fz Support	↑	+	+	=	=	
		CPU Time	↓	++	=	++	=	

The modelling properties of the rack system determine the transmission of internal forces (i.e. the shape and duration of the impulses) and therefore the energy exchanges. Hence, they modify the energy distribution within the racks affecting the mode of response and the final outputs. On the one hand, the friction coefficient and the rack-pool contact stiffness have a direct influence on the sliding/rocking response mode. On the other hand, the fuel-cell contact stiffness, the fuel gap and the fuel flexibility control the recurrence and magnitude of the fuel rattling inside the storage cell. However, both motions are closely related and may produce resonances. It is the overall balance of natural frequencies among rack body, fuel assemblies, and contacts which determines whether these rattling effects propagate to the rack supports or only cause local deformations.

The friction coefficient at the contact between rack support and pool liner determines the coupling between the first and the second. Such a coupling determines the manner the pool shaking energy in transmitted to the rack units. When this frictional coupling outweighs the water coupling effect, rocking motion becomes the preponderant response due to the momentum unbalance. In the opposite scenario where eccentric frictional forces are exceed by the centred hydrodynamic pressure, rack units tend to slide.

The rack-pool contact stiffness determines the penetration of the rack support into the pool liner and therefore the delay of the reaction. Stiff contacts boost the impact forces on supports and develop faster and higher frictional forces. Such early friction stops relative sliding facilitating the rocking response. Moreover, sharp reactions increase the computation cost as more and shorter steps are required to achieve convergence, especially when fuel contacts are also stiff.

Stiffness of the interior cylindrical contacts between fuel assemblies and storage cell determine the penetration of the first into the second. Stiff contacts reduce penetration at the upper contacts which may avoid the activation of lower contacts and bring computational savings. This concentration of high leverage impacts should assist the rocking behaviour, but numerical results point out controversial effects. Actually, sharp contacts produce rebounds and deformations of the fuel elements that may reduce the amount of energy transferred to the rack unit and consequently the sliding displacements and vertical forces on support. This dissipative effect depends on the size of fuel gaps and the violence of the rattling rose from rack-pool contact stiffness.

The fuel-cell gap determines the amplitude of the fuel rattling and therefore the recurrence and magnitude of the impacts. Moreover it defines the angle of inclination of the fuel bundle during the impact which influences the number of contacts to activate. Wide gaps allow the enclosed water to damp the relative motion prior to the impact resulting in smooth and progressive energy transferences. It pushes to a sliding-predominant behaviour especially when dealing with rigid fuel assemblies. However, wide gaps concentrate impacts at the top of the rack while lower contacts are rarely activated. It brings computation savings, but leads to a rocking response.

The relationship between the flexural flexibility of fuel assemblies and storage cell is essential to understand the rattling effects. Their relative deformations influence the number of contacts activated. Rigid assemblies do not deform after hitting the cell wall, so impact forces are concentrated at the upper contacts leading to a rocking-preponderant response. Flexible assemblies deform more than the rack cells, sticking to the wall and pushing to a sliding response. In addition, computation time falls down since most of the lower contacts remain inactive.

To sum up, eccentric forces with strong and sharp pulses generally lead to a rocking-predominant motion whereas soft and progressive forces acting close to the centre of masses give the ensemble the time to accelerate and to undergo sliding motion. Numerical outcomes are associated to the type of primary response. Rocking behaviour results in slight slidings and strong vertical forces on support due to the uplifts associated to the tilting. However, the computational cost time strictly depends on the number of active contacts solved throughout the transient analysis. Uplifts release alternative support contacts during rocking and concentrated rattling disuse lower fuel contacts.

5 Sobol indices

The Sobol method is a variance-based sensitivity analysis that decomposes the variance of the output data into fractions that can be attributed to the input variables. Figure 14 gives an idea at first sight of the weight of the modelling properties in each of the three main outputs. It is highlighted that sliding displacements (a) and CPU time (c) are strongly influenced by the friction coefficient whereas the vertical force on support (b) rely on the rack-pool contact stiffness.

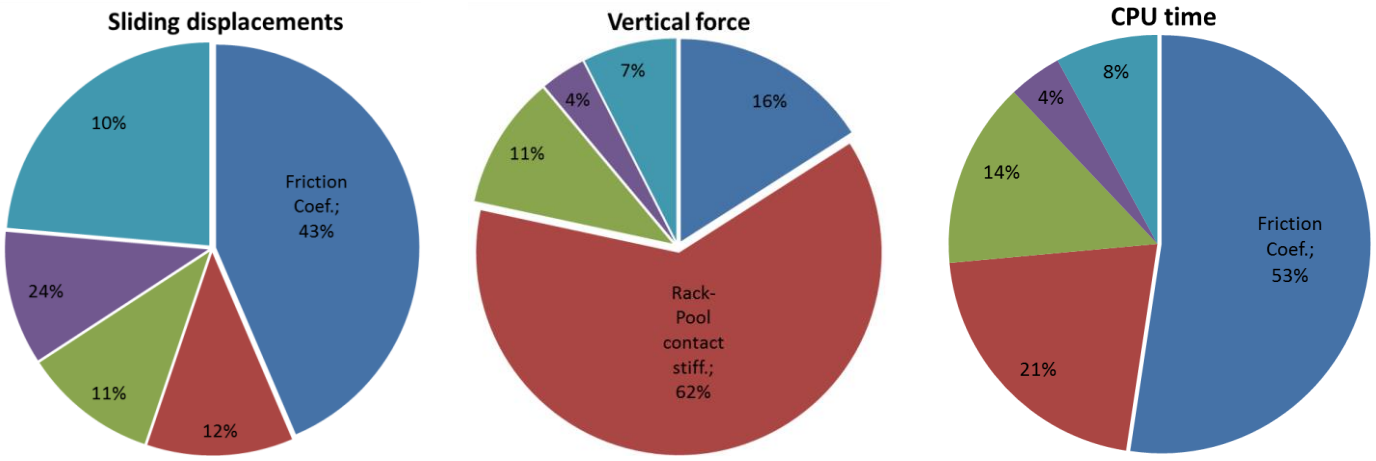

Figure 14 Total Sobol index for (a) Max. sliding displacements, (b) Max. vertical forces, (c) Computation time

6 Conclusions

During a seismic event, rack units undergo a volatile combination of three main types of motion: (a) coupled response together with the pool, (b) sliding displacement over the pool liner and (c) rocking oscillation around the vertical position. At the same time, fuel elements rattle inside their storage cells hitting the cell walls alternatively. Since these impacts are concentrated on the top of the rack, their high leverage strongly contributes to the overturning moments boosting the rocking behaviour.

These fuel and rack motions involve frequent contacts with important energy exchanges affecting the balance of forces. Moreover, both motions are influenced by the fluid-structure interaction and the water coupling effect that opposes the relative motion between wet boundaries, pushing for an in-phase motion. Hence, the modelling properties related these elements are decisive in the balance of energies and certainly affect the mode of response of the system. It is shown that minor changes in the model propagate throughout the transient analysis leading to large deviations in the final outputs. The following conclusions can be drawn from the simulations:

- The friction coefficient between rack support and pool liner determines the main mode of response of the units. Sliding response is dominant for low friction whereas rocking is associated to high friction. The kinetic energy consumed in the support uplifts of the rocking motion is deducted from the slidings. Since both modes of response are complementary, it is not possible to provide a safe value for the friction coefficient.
- Fuel rattling and rack rocking are closely related and can generate resonances. The balance of natural frequencies among fuel assemblies, rack structure and contacts stiffnesses determines whether the rattling energy reaches the rack supports or it is dissipated through local deformations. Stiff racks exhibit a rigid solid motion where any displacement at the top of the cantilever is reflected on the pedestal. Otherwise, in flexible racks the pedestal does not notice the deformation of the cantilever.
- The energy exchanges associated to the rattling are controlled by the fuel beam rigidity, the fuel-cell gap and the fuel-cell contact stiffness. Rigid fuel assemblies, wide gaps and stiff fuel contacts lead to strong impacts at the upper contacts located at the top of the storage cell while lower contacts remain inactive. It results in sharp and eccentric high frequency pulses leading to a rocking behaviour. Oppositely, deformable fuel bundles, tiny gaps and weak contacts lead to multiple soft contacts along the entire rack height. Fuel assemblies fold and deform up to stick to deformed rack body beam along the entire height driving to low energy pulses pushing the rack unit to a sliding response.
- Contact stiffness determines the magnitude and duration of the impact pulses. For instance, the stiffness of rack-pool contact is key in the maximum force at support. Use minimum amount of contact-compliance needed to remove spurious high frequency oscillations and prevent contact reversal.
- The computational cost time is highly sensitive to the number of active contacts solved throughout the transient analysis and to the roughness of their associated impacts. Rocking behaviour alternatively release

support contacts reducing the stiffness matrix. Sharp contacts cause costly oscillations requiring more and shorter steps to achieve convergence.

7 Acknowledgment

This project has received funding from the European Union's Horizon 2020 research and innovation programme under the Marie Skłodowska-Curie grant agreement No. 642453 (http://trussitn.eu). The authors would like to express their sincere gratitude to Phimeca for kindly providing technical support and the license of Phimecasoft.

8 References

ANSYS, Inc. 2012. ANSYS QA2012-01.

ANSYS, Inc., 2013. ANSYS Mechanical User's guide; Release 15.0

Ashar H, DeGrassi G., 1989. Design and analysis of free-standing spent fuel racks in nuclear power plants (an overview). 10th International Conference on Structural Mechanics in Reactor Technology, SMiRT 1989; CONF-890855—43, BNL-NUREG-42667.

Champomier F., Delemontey R., Sollogoub, P., Toumbas D., 1989. Seismic design of a spent fuel storage rack. 10th international conference on Structural Mechanics in Reactor Technology (SMIRT). CONF-890855; 589-594

Champomier F., Peron J.Y., 2001. Seismic justification of free standing spent fuel storage racks: experimental versus computed behaviour. 9th International conference on nuclear engineering.

Chung H, Chen S., 1984. Hydrodynamic mass. United States Government. CONF-840647—9.

DeGrassi G., 1992. Review of the technical basis and verification of current analysis methods used to predict seismic response of spent fuel storage racks, NUREG/CR-5912, BNL-NUREG-52335.

Fritz R.J., 1972. The effect of liquids on the dynamic motions of immersed solids. Journal of engineering for industry. 167-173

Gonzalez, A., Costas, L., Gonzalez, A. 2017. Parametric analysis of modelling properties governing the seismic response of free-standing spent fuel racks. European safety and reliability conference (ESREL)

Hinderks M, Ungoreit H, Kremer G., 2001. Improved method to demonstrate the structural integrity of high density fuel storage racks. Nuclear Engineering and Design. 206:177-184.

Lee G.M., Kim K.S., Park K.B., Park J.K., 1998. Three-dimensional seismic analysis for spent fuel storage rack. Journal of the Korean Nuclear Society. 30:91-98

Oh J. H., Ryu, J.S., 2013 Impact analysis for fuel assemblies in spent fuel storage rack. International group on research reactors, IGORR 2013

Queval JC, Sollogoub P, Champomier FP, Vallat S., 1999. Seismic behaviour of spent fuel storage racks. 15th International conference on Structural Mechanics in reactor Technology, (SMiRT)

Rabinowicz, E. 1976, "Friction Coefficients of Water-lubricated stainless steel for a spent fuel rack facility", Massachusetts Institute of Technology.

Soler, A., Singh K.P. 1984. Seismic response of a free standing fuel rack construction to 3-D floor motion. Nuclear engineering and Design, 80, 315-329.

Soler, A.I., Singh, K.P. 1982. Dynamic coupling in a closely spaced two-body system vibrating in a liquid medium: the case of fuel racks, 3rd Keswick International conference in nuclear plants.

Zhao Y, Wilson PR, Stevenson JD. 1996. Nonlinear 3-D dynamic time history analysis in the reracking modification for a nuclear power plant. Nuclear Engineering and Design. 165:199-221.

Zhao Y., 1997. Finite element modelling and analysis of nonlinear impact and frictional motion response including fluid-structure coupling effects. Shock and vibration. 4:311-325.

U.S. Nuclear Regulatory Commission, 1981. 'Standard Review Plan for the review of safety analysis reports for nuclear power plants. Chapter 3– Design of structures, components, equipment and systems'. NUREG-0800, formerly issued as NUREG-75/087.

Hilbert H.M., Hughes T.J.R., Taylor R.L., 1977. Improved numerical dissipation for time integration algorithms in structural dynamics. Earthquake engineering and structural dynamics; 5:283-292.

Gonzalez, A., Costas, L., Gonzalez, A. 2017. Parametric analysis of modelling properties governing the seismic response of free-standing spent fuel racks. European safety and reliability conference (ESREL)